Transp Porous Med
https://doi.org/10.1007/s11242-018-1072-8

Immobile Pore-Water Storage Enhancement and Retardation of Gas Transport in Fractured Rock

Dylan R. Harp[1] · John P. Ortiz[1] · Sachin Pandey[1] · Satish Karra[1] · Dale Anderson[2] · Chris Bradley[2] · Hari Viswanathan[1] · Philip H. Stauffer[1]

Received: 27 November 2017 / Accepted: 26 April 2018

Abstract The effect of immobile pore-water on gas transport in fractured rock has implications for numerical modeling of soil vapor extraction, methane leakage, gaseous CO_2 leakage from sequestration operations, radionuclide transport from underground nuclear explosions, and nuclear waste disposal. While the ability for immobile pore-water storage to effect gas transport has been recognized in the past, the details and specific scenarios leading to enhanced, retarded, or unaffected gas transport have not been explored. We performed numerical investigations into the enhancement and retardation of gas transport due to immobile pore-water storage in order to identify implications for gas transport applications. To do this, we developed a numerical approach to model gas transport with a single-phase flow solution coupled to the advection–dispersion equation modified to account for immobile pore-water storage. Other than the immobility of pore water, the formulation contains all other physics included in two-phase formulations (advective and diffusive gas transport in fractures and rock matrix and dissolution in immobile pore water). The assumption of immobile pore water is valid here since for many applications involving transport of soluble gases in fractured rock, the rate of aqueous transport is insignificant compared to gas transport. We verify our modeling approach with analytical solutions of: (1) 1D gas diffusion, (2) 1D gas advection, (3) barometric pumping of a fracture, and (4) gas transport with uniform fracture flow and diffusion into the matrix. We account for pore-water storage in our model by implementing a kinetic formulation of gas dissolution wherein the dissolved (aqueous) phase is considered an immobile constituent. Using this formulation, we model the effect of dissolution rate and saturation on the retardation of gas transport during pure diffusion and pure advection. We also demonstrate that although it is commonly believed that pore-water storage will always enhance gas transport in fractures during oscillatory flow (e.g., during reversing pressure gradients such as barometric pumping cycles), our simulations indicate

✉ Dylan R. Harp
dharp@lanl.gov

[1] Computational Earth Science Group, Los Alamos National Laboratory, Los Alamos, NM 87544, USA

[2] Geophysics Group , Los Alamos National Laboratory, Los Alamos, NM 87544, USA

Published online: 10 May 2018

that this may not always be the case. Our numerical investigations indicate that scenarios with lower effective diffusion coefficients ($\lessapprox 10^{-5}$ m^2/s) and lower dissolution coefficients (i.e., the dissolution diffusion coefficient) ($\lessapprox 10^{-11}$ m^2/s) will result in enhanced gas transport. Other combinations of gaseous diffusion and dissolution coefficients result in delayed gas transport or insignificant effect on gas transport. Based on these results, and given the fact that the free-air diffusion coefficients for many gases are slightly above 10^{-5} m^2/s (near the boundary of enhanced/non-enhanced gas transport), tortuosity would have to be significant for gas transport enhancement to occur. Similarly, if we consider the free-water diffusion coefficient of gases (around 10^{-9} m^2/s for many gases of interest) to be a maximum bound for the effective dissolution coefficients (i.e., the rate of diffusion into the water away from the air/water interface will limit the dissolution rate), the effective dissolution coefficient would have to be at least 2 orders of magnitude less for enhanced gas transport to occur. Otherwise, pore-water storage will delay or have negligible effect on the gas transport. The results also indicate that the assumption of instantaneous equilibrium, often invoked in numerical codes for dissolution processes (i.e., dissolution coefficient is effectively infinite), will fail to accurately capture important details of soluble gas transport. The implication of our results is that gas breakthrough times in fractured rock during oscillatory flow may be highly dependent on the effective gaseous diffusion and dissolution coefficients.

Keywords Fracture flow · Gas transport · Dissolution · Barometric pumping

1 Introduction

The ability to efficiently and accurately model gas transport in fractured rock in the presence of pore water is important for a variety of practical applications ranging from radionuclide transport from underground nuclear explosions (Carrigan et al. 1996; Bowyer et al. 2002; Issartel and Baverel 2003; Carrigan and Sun 2014; Sun and Carrigan 2014; Jordan et al. 2014, 2015; Carrigan et al. 2016), passive vapor extraction of volatile contaminant plumes (Rathfelder et al. 1995; Auer et al. 1996; Ellerd et al. 1999; Stauffer et al. 2005; Neeper and Stauffer 2005), leakage from carbon sequestration sites (Oldenburg and Unger 2003; Viswanathan et al. 2008; Shukla et al. 2010; Pan et al. 2011; Dempsey et al. 2014; Carroll et al. 2014), and methane extraction and leakage due to hydraulic fracturing (Myers 2012). While a large body of research exists on the flow of gases in fractured rock (Grisak and Pickens 1981; Nilson and Lie 1990; Nilson et al. 1991; Wyatt et al. 1995; Auer et al. 1996; Neeper 2002; Ho and Webb 2006), the effects of kinetic pore-water storage on gas transport in fractured rock have not been investigated in detail. While the existence of pore water with a constant pressure gradient is known to delay transport, the existence of pore water with oscillatory flow (i.e., barometric variations) has been assumed to enhance transport due to a ratcheting mechanism. In this paper, we demonstrate numerically the potential for pore-water storage in a fractured rock subjected to barometric variations to enhance or retard gas transport depending on the gaseous and dissolution diffusion coefficients. The dissolution diffusion coefficient quantifies the rate of diffusion across the air/water interface boundary layer and will be referred to as the *dissolution coefficient* throughout this paper. While we focus on the effect of pore-water storage on gas transport, similar effects may occur for other types of oscillatory flow systems involving mobile/immobile components, such as the mobile gas/immobile gas system described by Neeper and Stauffer (2012).

In all but the most extreme cases, aqueous (pore-water) transport is insignificant compared to gas transport in unsaturated, fractured rock (Nilson et al. 1991). Fractures in unsaturated

rock are expected to drain, allowing gas transport to dominate along these conduits, relegating aqueous transport to the intact rock matrix (Ho and Webb 2006, Chapter 23). Additionally, due to the lower viscosity of air, air flow will be much larger than water flow when subjected to the same pressure gradient (Brusseau 1991). Gas flow through fractures driven naturally by barometric pumping can be on the order of a few m/day (Sun and Carrigan 2014), while unsaturated groundwater flow can easily be 1 mm/day or slower, particularly within the rock matrix of rocks that are amenable to fracturing (e.g., granitic rocks, welded tuffs). Unsaturated rock with large saturation and significant permeability is generally in the transient process of draining through the rock matrix and possibly the fractures. However, tighter rock, such as many granitic rock with low permeability (0.001 mD), may have large saturation with little drainage through the fractures occurring. The larger saturations investigated here are relevant for this latter case.

A large infiltration event could lead to significant downward movement of water; however, in all but the most extreme cases, this scenario's effect would be restricted to the shallow subsurface while many gas transport applications will involve much greater depths. Scenarios with upward groundwater flow from depth leading to significant aqueous transport compared to gas transport will occur even less frequently. Evapotranspiration will cause upward pore-water movement; however, even with a large evaporative potential, this would only affect the first few meters below the ground surface.

Considerations such as the preceding arguments indicate that it is reasonable to neglect aqueous transport in many practical gas transport applications, especially when the majority of the transport is more than a few meters below the ground surface. However, the aqueous phase cannot be completely ignored as it provides a storage mechanism for gas transport. Soluble gases at low concentrations will partition between aqueous and gaseous phases as governed by Henry's Law. In most cases, this will result in retardation of gas transport. However, in specific cases with oscillatory flow, aqueous storage can enhance gas transport compared to gas transport without aqueous storage (such as the idealized case where no pore water is present). This occurs because gas transport is not completely reversed during flow reversals, i.e., the upward advance during barometric lows is partially maintained in pore-water storage. Therefore, while we can neglect *aqueous transport* in most cases, we cannot ignore *aqueous (pore-water) storage* due to its ability to retard and enhance gas transport. Figure 1 provides a simplified illustration of this process, where gas diffuses into the rock matrix and dissolves into the pore water during barometric highs and volatilizes and diffuses back into the fracture during barometric lows. Our formulation captures the physical processes illustrated in Fig. 1.

We develop an approach to model gas transport in unsaturated, fractured rock using a single-phase flow solution coupled to a modified advection–dispersion equation that accounts for immobile pore-water storage. The approach fills a gap in subsurface, soluble gas transport simulation capability, since most simulators focus more on transport involving aqueous/solid species than on gases. We developed our approach in the PFLOTRAN simulator (Lichtner et al. 2015), which will allow for massively parallel simulations and discrete fracture network simulations (Hyman et al. 2015). We account for pore-water storage by implementing a kinetic formulation of gas dissolution where the dissolved (aqueous) phase is considered an immobile constituent. Conceptually, this is similar to modeling an adsorption process where a substance adheres to immobile solid particles. Other than the assumption of immobile pore water, the formulation captures all other features of two-phase formulations, including advective and diffusive gas transport in both fractures and rock matrix and kinetic dissolution/volatilization in pore water.

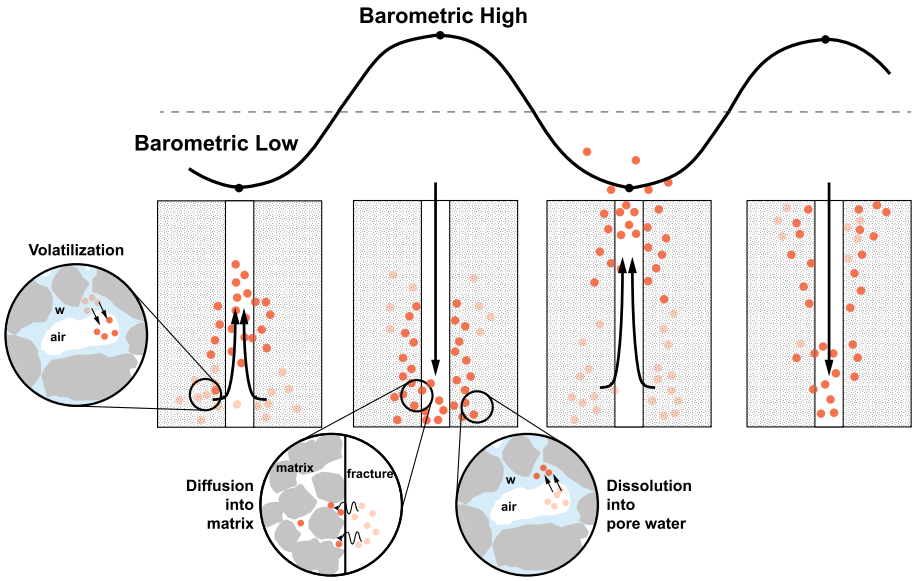

Fig. 1 Schematic of the process of enhanced gas transport due to pore-water storage during barometric pumping. The advance of the gas during barometric lows is not completely reversed during subsequent barometric highs due to storage of dissolved gas in rock matrix pore-water

The formulation may be considered a dual-porosity formulation (Chen 1989) involving mobile and immobile porosity. However, in implementation, it is more similar to sorption formulations where the sorbed phase is accounted for as an immobile chemical constituent. In our formulation, the gaseous flow and transport within the fractures and matrix are represented using a single continua, and the immobile aqueous phase is represented as an immobile chemical constituent. The water-filled porosity is not explicitly represented, but accounted for in the determination of the added chemical constituent concentration (i.e., the aqueous phase concentration).

In Sect. 2, we describe our modeling approach. Since, to our knowledge, this is the first application of PFLOTRAN to model gas flow and transport, in Appendix A, we ensure that the approach is consistent with fundamental equations of gas flow and transport. We verify our approach against analytical solutions of: (1) 1D gas diffusion, (2) 1D gas advection, (3) sinusoidal barometric pumping of a fracture, and (4) gas transport along a fracture with uniform flow and diffusive walls. We demonstrate and verify our kinetic dissolution formulation in Sect. 3.1. In Sect. 4, we use our formulation to explore the effect of pore-water storage on gas transport for (1) 1D gas diffusion, (2) 1D gas advection, and (3) barometric pumping of a gas in a single fracture. In Sect. 5, we discuss the implications of our results within the context of gas transport applications and in Sect. 6, we provide conclusions.

2 Methods

2.1 Single-Phase Flow and Reactive Transport Model

We model air flow with the single-phase flow equation

$$\phi_a \frac{\partial \rho_a}{\partial t} + \nabla \cdot (\rho_a \mathbf{q}) = Q, \tag{1}$$

where ϕ_a is air-filled porosity, ρ_a is air density, Q is a flow source/sink term, t is time, and $\mathbf{q}$ is Darcy (volumetric) flux defined as

$$\mathbf{q} = -\frac{k}{\mu}\nabla(p - \rho_a g z), \tag{2}$$

where k is the permeability, μ is the pneumatic viscosity, g is the gravitational constant, and z is the vertical coordinate.

We use an exponential relationship to describe the equation-of-state for the effect of pressure on air density as

$$\rho_a(p) = \rho_{a,0} \exp(\beta(p - \overline{p}_0)), \tag{3}$$

where $\rho_{a,0}$ is the reference air density (1.225 kg/m^3), β is the compressibility of air (9.87×10^{-6} Pa^{-1}), and $\overline{p}_0$ is the mean static barometric pressure.

We couple the single-phase gas flow equation to the advection–dispersion equation (ADE) defined as

$$\phi_a \frac{\partial C_g}{\partial t} + \nabla \cdot (\mathbf{q} C_g - \phi_a \tau D^* \nabla C_g) = Q_c, \tag{4}$$

where C_g is the gas concentration, τ is tortuosity, D^* is the molecular diffusion/dispersion coefficient, and Q_c is the transport source/sink term.

In our research, we utilize PFLOTRAN's single-phase flow solver (Richards' equation solver with air properties and (air) saturation fixed at unity) and its ADE solver to solve the equations above.

2.2 Kinetic Dissolution Formulation

We added a kinetic formulation of dissolution with equilibrium partitioning governed by Henry's Law. The kinetic formulation allows the details of dissolution/volatilization to be explicitly modeled by including the dissolution coefficient, interfacial area, and boundary layer thickness. This formulation allows us to investigate the effect of dissolution rate on gas transport. The kinetic formulation also allows us to evaluate the validity of the "instantaneous equilibrium" assumption often used for dissolution in numerical codes, shown to be inadequate here, to capture the details of pore-water storage on gas transport.

We developed the kinetic formulation in PFLOTRAN's Reaction Sandbox (Hammond 2015), a framework for implementing user-defined reactions within PFLOTRAN. The dissolution rate formulation is based on Fick's first law of diffusion as

$$N_i = -D_d \nabla C_i \tag{5}$$

where N_i is the molar flux of the ith species, D_d is the dissolution coefficient (sometimes referred to as the small-scale diffusion coefficient), and C_i is the concentration of the ith species. In our formulation, within each cell, we model the molar flux between the gas and aqueous phases as zero-spatial dimensional transfer between two reservoirs (i.e., the air and water). Based on this geometrical configuration, the molar flux N_i can be expanded into the temporal rate of change in the number of moles per unit area as

$$N_i = \frac{1}{A}\frac{\mathrm{d}m_i}{\mathrm{d}t}, \tag{6}$$

where A is the interfacial area between the air and water and m_i is the number of moles of the ith species. The gas phase concentration that would be required for equilibrium given the current aqueous phase concentration at any time, C_{g}^{s}, can be expressed as

$$C_{\mathrm{g}}^{s} = \frac{C_{\mathrm{w}}}{H_{\mathrm{c}}}, \tag{7}$$

where H_{c} is the dimensionless Henry's coefficient ($H_{\mathrm{c}} = C_{\mathrm{w}}/C_{\mathrm{g}}$), and C_{g} and C_{w} are the gas concentrations in the air and pore water, respectively. Therefore, the concentration gradient in Eq. 5 that will be exerted on the gas phase across the boundary layer d (i.e., the thin layer that dissolution/volatilization transports mass across) can be expressed as

$$\nabla C_{\mathrm{g}} = \frac{C_{\mathrm{g}} - \frac{C_{\mathrm{w}}}{H_{\mathrm{c}}}}{d}. \tag{8}$$

Substituting Eq. 6 (for the gas species) and Eq. 8 into Eq. 5 and multiplying through by A produces

$$\frac{\mathrm{d}m_{\mathrm{g}}}{\mathrm{d}t} = \frac{A}{d} D_{\mathrm{d}} \left(C_{\mathrm{g}} - \frac{C_{\mathrm{w}}}{H_{\mathrm{c}}} \right), \tag{9}$$

which is equivalent to the Noyes–Whitney dissolution equation (Noyes and Whitney 1897) applied to dissolution/volatilization of a soluble gas. The volatilization rate equals the negative of the dissolution rate (i.e., $\mathrm{d}m_{\mathrm{w}}/\mathrm{d}t = -\mathrm{d}m_{\mathrm{g}}/\mathrm{d}t$). This formulation ensures that the ratio of aqueous and gas phase concentrations will asymptotically approach the Henry's coefficient of the gas in accordance with Fick's first law of diffusion.

As mentioned above, while we use PFLOTRAN's Richards solver, it is run in air-saturated conditions so that the porosity specified is effectively the air-filled porosity (ϕ_{a}). The water-filled porosity (ϕ_{w}) is accounted for internally in the formulation by converting the bulk concentration (C_{b}) used in calculations by PFLOTRAN for the immobile constituent in each cell to the aqueous concentration as

$$C_{\mathrm{w}} = \frac{C_{\mathrm{b}}}{\phi_{\mathrm{w}}} \tag{10}$$

prior to calculating the rate in Eq. 9. In this way, although pore water is not explicitly modeled in the flow solver, immobile pore-water storage is accounted for in the transport. This approach is a computationally efficient way to model gas transport compared to full, multiphase solutions that include the effects of pore-water storage. Conceptually, this is similar to modeling adsorption onto immobile solid particles. Other than the immobility of the pore water, all other aspects of a two-phase formulation are included (gaseous diffusion and advection in fractures and rock matrix and dissolution/volatilization in pore water).

3 Benchmarking and Verification

Since this is the first application of PFLOTRAN to model gas transport during barometric pumping, we benchmark the formulation against existing analytical solutions in Appendix A, including (1) 1D gas diffusion, (2) 1D gas advection, (3) barometric pumping of a fracture, and (4) gas transport with uniform fracture flow and diffusion into the matrix. In this section, we verify our kinetic dissolution formulation.

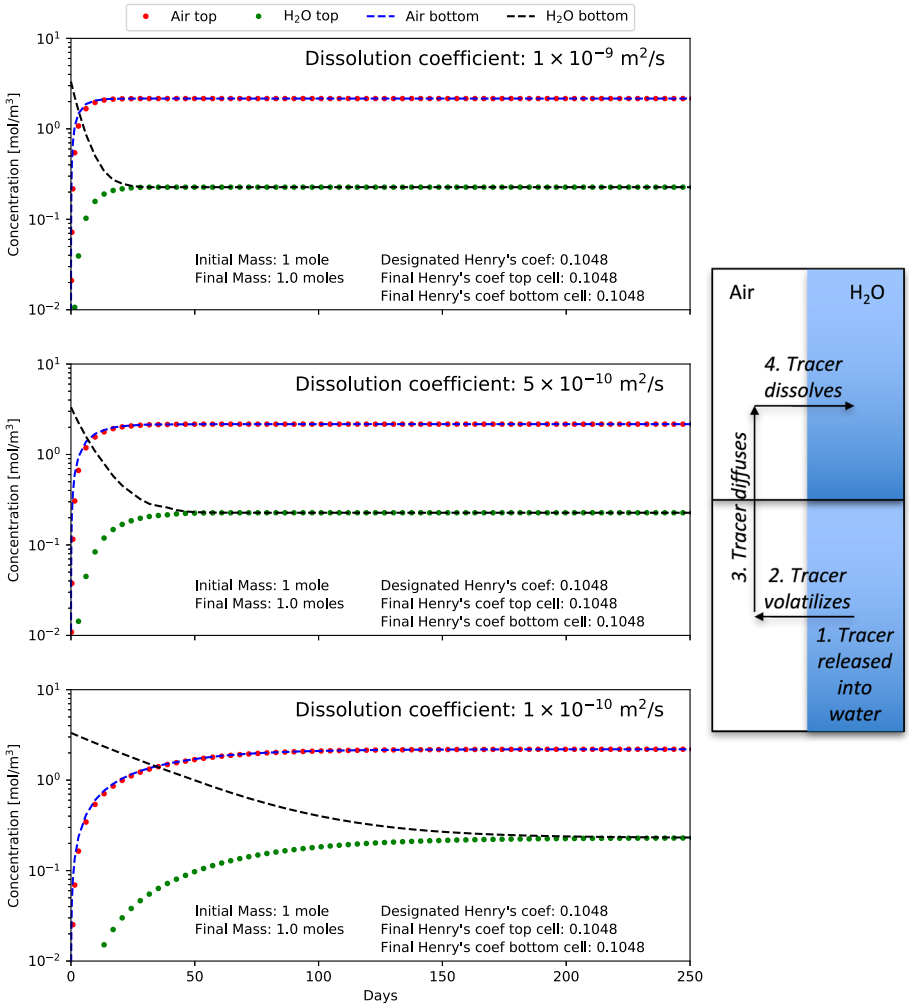

Fig. 2 Demonstration of gas tracer dissolution/volatilization governed by Henry's Law partitioning in a closed system described by the schematic on the right. The plot on the left contains the concentrations in the aqueous and gas phases in the top and bottom cells for dissolution coefficients 10^{-9}, 5×10^{-10}, 10^{-10} m^2/s. The final mass and Henry's coefficients indicated are automatically calculated for each simulation

3.1 Verification of Kinetic Dissolution Formulation

To verify our kinetic dissolution formulation, we constructed a closed boundary numerical simulation (i.e., all boundaries are no-flow) of two vertically stacked cells. The total porosity ϕ is 0.5, with 0.2 air-filled ϕ_a and 0.3 water-filled ϕ_w porosities. One mole of conservative gas tracer is released into the water in the bottom cell. The gas then volatilizes into the air in the bottom cell, where it can diffuse into the air of the top cell, and ultimately dissolve into the water of the top cell. The right side of Fig. 2 illustrates the processes schematically. The simulation results in equilibrium diffusion of gas between the two cells and Henry's Law partitioning between gas and aqueous phases, where the Henry's coefficient in dimensionless form is 0.1048 (the Henry's coefficient of xenon).

The left side of Fig. 2 contains time series of gas and aqueous concentrations in the model where the diffusion coefficient is 10^{-5} m^2/s and with dissolution coefficients of 10^{-9}, 5×10^{-10}, 10^{-10} m^2/s. The formulation conserves gas tracer mass, as indicated in the plots, where the final calculated masses are noted. The formulation also adheres to Henry's law partitioning, where the calculated dimensionless Henry's coefficient in the top and bottom cell are also indicated, where Henry's coefficient is calculated as $H_c = C_w/C_g$ using the concentrations at the end of the simulations. This demonstrates that the formulation is adhering to rate-limited dissolution/volatilization according to Fick's law (Eq. 9).

4 Results

Gas transport in fractured rock with immobile pore-water storage is relevant for many practical applications including: methane extraction from hydraulic fracturing operations and the potential leakage from such operations, volatile organic compound vapor extraction operations, shallow leakage of CO_2 from geologic sequestration operations, and radionuclide gas seepage from underground nuclear explosions or nuclear waste storage operations (e.g., xenon gas). In this section, we investigate a range of gaseous diffusion and dissolution coefficients (along with varying levels of saturation) to explore their effects on gas transport. We use the numerical models benchmarked and verified in Appendix A and Sect. 3 to investigate the effects of kinetic dissolution for (1) 1D gas diffusion, (2) 1D gas advection, and (3) gas transport in a single fracture subjected to barometric pumping.

4.1 Delayed Gas Transport During Pure Diffusion

We investigated the effect of immobile pore-water storage with kinetic dissolution on gas transport during pure diffusion by running a parameter study of simulations using our formulation. The analytical solution, used for reference here, and the PFLOTRAN model are identical to those described in Section A.1, except that the PFLOTRAN model includes our kinetic dissolution formulation. In Fig. 3, we present results from the parameter study, where the dissolution coefficient D_d and water-filled porosity ϕ_w are varied. We also varied the diffusion coefficient D^* from 10^{-10} to 10^{-6} m^2/s, but this only scaled the results without changing their general character. Therefore, we only show the results for $D^* = 10^{-6}$ m^2/s.

The dashed line in each of the plots is the analytical solution (Eq. 14) which only considers the case without pore water ($\phi_w = 0$). At $D_d = 10^{-14}$ m^2/s (top plot in Fig. 3), there is very little retardation apparent at any saturation. As D_d increases, the retardation increases as the tracer is more readily dissolved in the pore water. Increasing the amount of pore water present by increasing ϕ_w also leads to increased retardation as the volume available to store the tracer in the aqueous phase increases. Increasing D_d above 10^{-10} m^2/s did not lead to significantly more transport retardation and is therefore not presented here.

4.2 Delayed Gas Transport During Pure Advection

We investigated the effect of pore-water storage with kinetic dissolution on gas transport during pure advection by running a parameter study of simulations using our formulation. The analytical solution, used for reference here, and the PFLOTRAN model are identical to those described in Appendix A.2, except that the PFLOTRAN model includes our kinetic dissolution formulation. In Fig. 4, we present the results of the parameter study varying the dissolution coefficient (D_d) and the water-filled porosity (ϕ_w). To minimize the effect

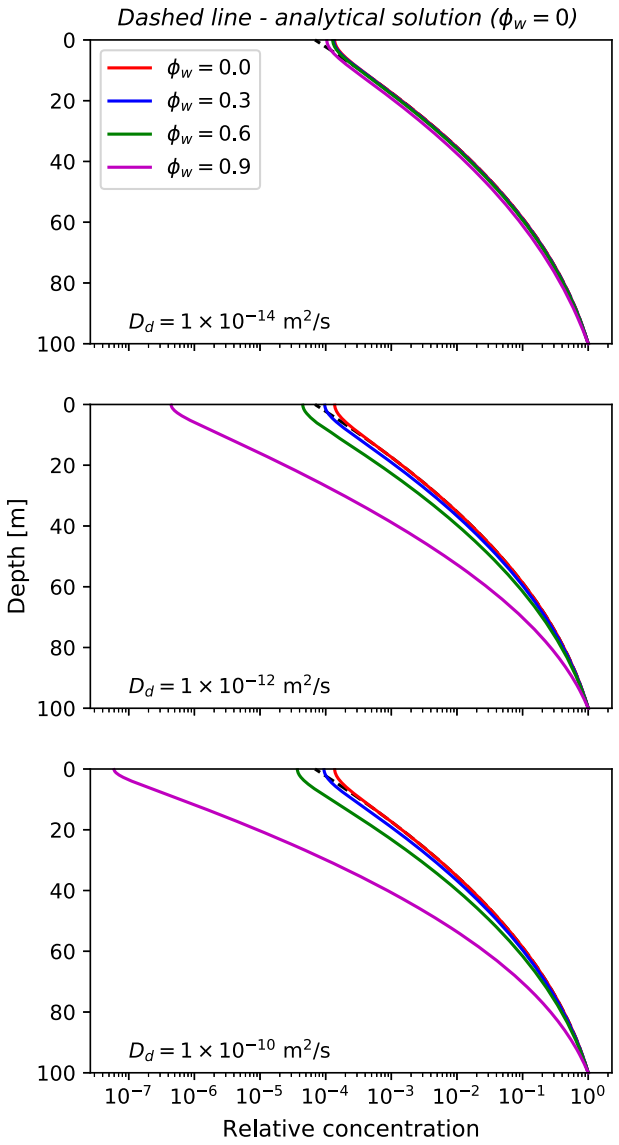

Fig. 3 Effect of pore-water storage on purely diffusive gas transport. Transects of relative concentration over depth (depth $= 100 - z$) for $\phi_w = 0,\ 0.3,\ 0.6,\ 0.9$ are compared for $D_d = 10^{-14}$ (top), $D_d = 10^{-12}$ (middle), and $D_d = 10^{-10}$ (bottom) m^2/s. The dashed black lines (predominantly obscured) are the corresponding analytical solution transects where $\phi_w = 0$ is implied

of numerical dispersion and isolate the effects of pore-water storage, we use the slowest volumetric flux and the most refined spatial and temporal resolutions from Appendix A.2 (a constant volumetric flux of $q_x = 0.01$ m^3/d/m^2, mesh spacing of $\Delta x = 1$ mm, and time step size of $\Delta t = 1$ h) and plot the concentrations at 10 years (refer to Figs. 11 and 12 and associated discussion in Appendix A.2). The red line in each plot of Fig. 4 is associated with no pore water and is identical to the red line in the top plot of Fig. 12.

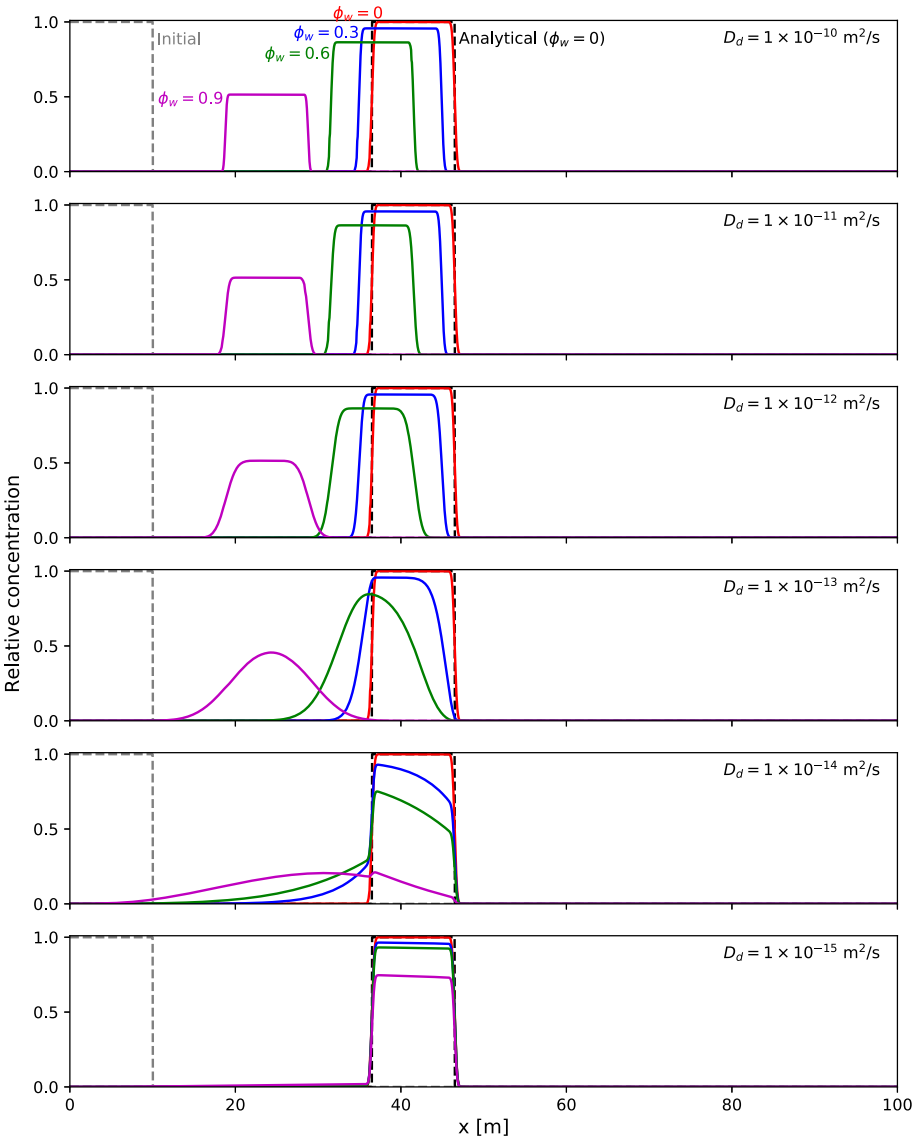

Fig. 4 Effect of immobile pore-water storage on advective gas transport. Relative concentrations at 10 years with a volumetric flux of 0.01 $m^3/d/m^2$ are compared in each plot for $\phi_w = 0,\ 0.3,\ 0.6,\ 0.9$ for dissolution coefficients (D_d) ranging from 10^{-10} to 10^{-15} m^2/s

Looking at the series of plots in Fig. 4, where D_d ranges from 10^{-10} to 10^{-15} m^2/s, the gas transport transitions from retarded transport with little dispersion ($D_d = 10^{-10}$ m^2/s), to retarded transport with plume dispersion ($D_d = 10^{-13}$ m^2/s), to no retardation or plume dispersion ($D_d = 10^{-15}$ m^2/s). Larger values of ϕ_w reduce gaseous concentrations since more volume is available for pore-water storage. The lack of retardation for low dissolution coefficient (i.e., $D_d = 10^{-15}$ m^2/s) indicates that the dissolution rate is too slow to significantly effect transport. In cases with plume dispersion (e.g., $D_d = 10^{-13}$ m^2/s), higher values of ϕ_w lead to greater dispersion.

Plume dispersion occurs for certain dissolution coefficients in Fig. 4 because of rate-limited transfer between the air and water. In the top plot ($D_d = 10^{-10}$ m^2/s), the dissolution/volatilization rate is practically instantaneous, and therefore, very little plume dispersion occurs. As the dissolution/volatilization rate decreases, the rate-limited transfer leads to increasing levels of plume dispersion and longer concentration tails. In the bottom plot ($D_d = 10^{-15}$ m^2/s), the dissolution/volatilization rate is so slow that although dissolution and volatilization are occurring, the rate of advection is outpacing the dissolution/volatilization, resulting in primarily plug flow (no dispersion). In this case, the loss of gaseous concentrations in the plume with increasing ϕ_w are nearly imperceptibly spread behind the plug-like plume. The transition toward the final plug-like flow in the bottom plot is apparent in the plot above ($D_d = 10^{-14}$ m^2/s) where long tails have formed.

4.3 Enhanced and Delayed Gas Transport During Oscillatory Flow

We investigated the effect of pore-water storage with kinetic dissolution on gas transport in a model with a single fracture subjected to oscillatory flow (barometric pumping) by conducting a Latin Hypercube Sampling (LHS) of simulations using our formulation. The simulations are similar to the PFLOTRAN simulations described in Appendix A.3, but include gas transport and pore-water storage. A conservative gas tracer is released at $t = 0$ uniformly across the bottom 10 meters of the model. Barometric pressure variations with period of 7.305 days and amplitude of 1000 Pa are applied along the top (ground surface) of the model.

The factors in the LHS and their ranges are matrix saturation $S \in [0 : 0.9]$ (where $S = \phi_w/(\phi_a + \phi_w)$), diffusion coefficient $D^* \in [10^{-7} : 10^{-4}]$ m^2/s, and dissolution coefficient $D_d \in [10^{-14} : 10^{-9}]$ m^2/s. 1000 parameter combinations were generated using LHS. We define pore-water transport enhancement TE for each parameter combination as the integral of the difference between the log relative concentrations at the top of the fracture for the simulation with the parameter combination and that of an associated simulation without pore water (i.e., setting $S = 0$) over 120 days as

$$\mathrm{TE}(\theta_i) = \int_0^{120\,\mathrm{days}} (\log_{10}(C_g(\theta_i)) - \log_{10}(C_g(\theta_i; S = 0)))\mathrm{d}t \tag{11}$$

where θ_i is the ith LHS parameter combination and $C_g(\theta_i; S = 0)$ is the simulation associated with $C_g(\theta_i)$ but with no pore water. Negative values of transport enhancement indicate transport retardation.

Figure 5 contains time series of relative concentrations in blue for the most enhanced (top plot) and most delayed (bottom plot) parameter combinations in the LHS sampleset. The associated concentrations without pore water (with $S = 0$) are shown in green. The gaseous diffusion and dissolution coefficients for the samples are indicated in each plot. The gray-shaded area between the curves indicates the area quantified by the transport enhancement metric in Eq. 11.

Our definition of transport enhancement maintains the total porosity in the matrix between the two simulations, while some of the air-filled porosity in the matrix is replaced with pore water (water-filled porosity). This allows for the comparison of the effect on gas transport at a particular site when the rock matrix changes from completely dry to partially saturated. Of course, this means that the porosity available for gas diffusion and advection in the matrix will change between the two simulations.

To illustrate the numerical simulations, we present simulated relative gas concentrations in Fig. 6 corresponding to the most enhanced case in Fig. 5. In the simulation, the gas is ratcheted toward the surface, as can be seen in moving along the plots from left to right. Gases are

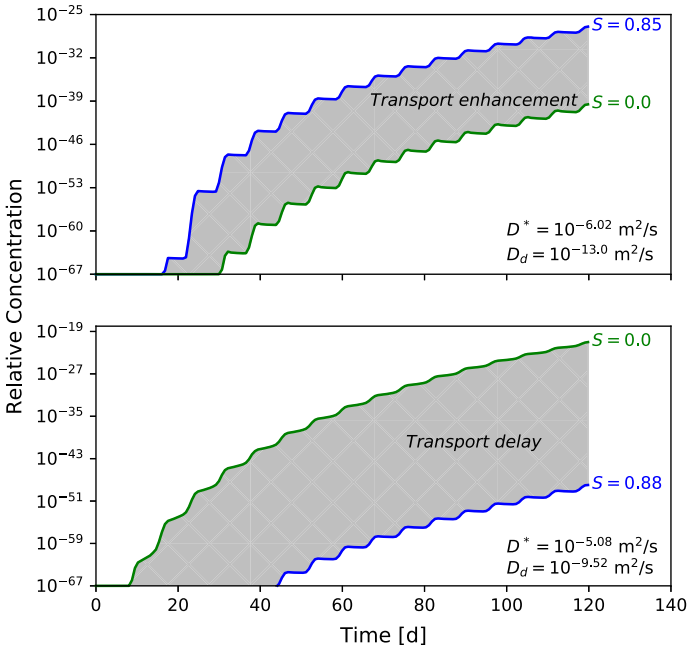

Fig. 5 LHS parameter combinations with the greatest transport enhancement (top) and transport delay (bottom). The diffusion coefficient D^* and dissolution coefficient D_d are indicated in each plot. The blue lines are the concentrations with pore water, while the green lines are the concentrations for the associated simulations without pore water. The lines are labeled by saturation S

pulled upwards in the fracture during barometric lows and pushed back downwards during barometric highs. In this case of enhanced transport, the upward migration of gas during barometric lows is maintained during barometric highs.

Given that gaseous and dissolution diffusive processes can be characterized by characteristic times (i.e., $t_\mathrm{c} = L^2/D$, where L is a characteristic length and D is the diffusion coefficient of the diffusive process of interest), a good question is how do these characteristic times relate to the period of the barometric pressure signal and how do changes in the barometric pressure period effect the transport enhancement. We use the depth of the fracture (100 m) and boundary layer thickness (0.01 m) as the characteristic length of gaseous diffusion and dissolution diffusion, respectively. The range of characteristic times considered in our ensemble is then around 10^3 to 10^6 days for gaseous diffusion (corresponding to $D^* = 10^{-4}$ to 10^{-7} m^2/s, respectively) and around 1.2 to 10^5 days for dissolution diffusion (corresponding to $D^* = 10^{-9}$ to 10^{-14} m^2/s, respectively).

In Fig. 7, we plot the transport enhancement for the most enhanced and delayed transport cases from Fig. 5 as a function of barometric pressure period. The range of barometric pressure periods covers periods associated with weather patterns. These results demonstrate that transport enhancement is insensitive to the barometric pressure period over the range associated with weather patterns, which are the dominant barometric pressure period driving gas transport. The delayed case (blue line) does show more variability than the enhanced case (red line), but the variations appear random without a discernible pattern and are likely due to changes in ending phase at 120 days used in the transport enhancement metric and not related to characteristic times.

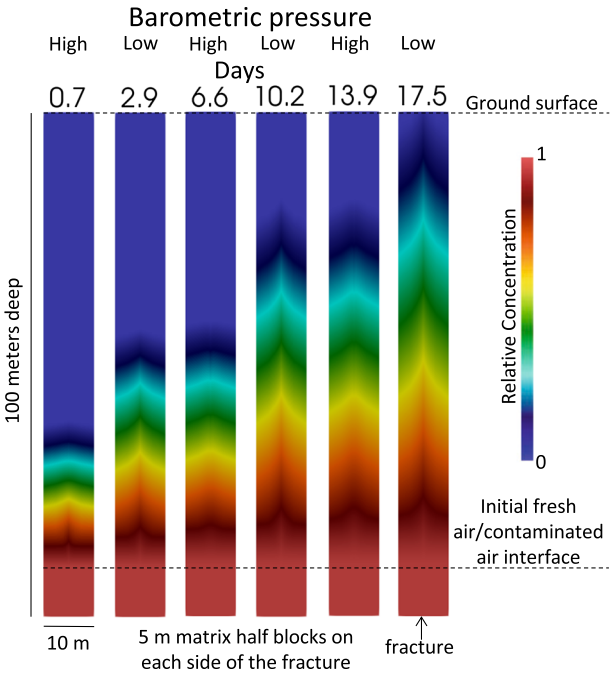

Fig. 6 Numerically simulated relative gas concentrations corresponding to the most enhanced case from Fig. 5. Relative gas concentration color maps are shown increasing in time from left to right. Actual simulations are half models include half of the 1-mm fracture attached to one 5-m matrix half-block. The results are reflected horizontally about the fracture in the images

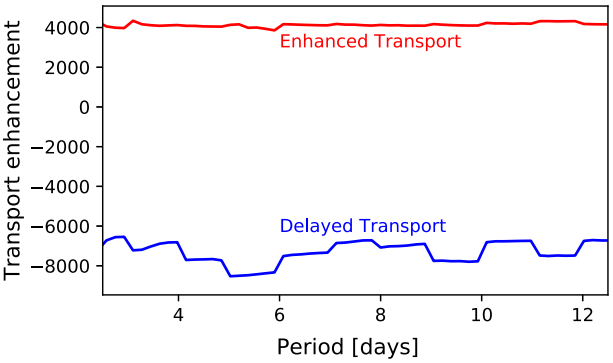

Fig. 7 Sensitivity of transport enhancement to barometric pressure period for the most enhanced and delayed simulations in the ensemble

The lack of sensitivity of transport enhancement to barometric pressure period is due to the fact that the characteristic time for gaseous diffusion is orders of magnitude larger than the barometric period. While for large dissolution coefficients, the characteristic time for dissolution diffusion does overlap with weather-pattern barometric periods, the gaseous and dissolution diffusive processes occur in series, where dissolution occurs after gaseous diffusion transports the gas into the rock matrix. Therefore, transport enhancement is not

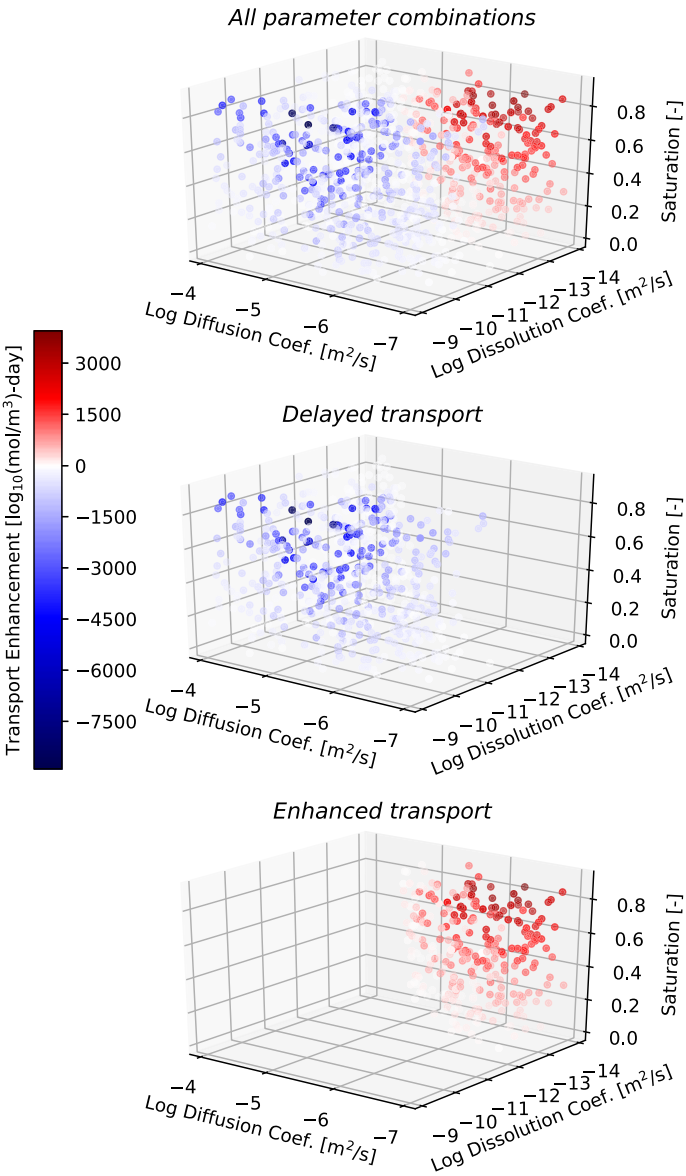

Fig. 8 3D scatterplots of the LHS ensemble colored by pore-water transport enhancement for all parameter combinations (top), delayed transport cases (middle), and enhanced transport cases (bottom). Darker shades of red indicate greater transport enhancement, darker shades of blue indicate greater transport delay, and cases with little effect on transport fade to white

dependent on the weather-pattern barometric pressure period because the barometric periods are much shorter than the characteristic time of gaseous diffusion.

Figure 8 contains 3D scatterplots of the LHS ensemble colored by transport enhancement. The top plot contains the entire ensemble, while the middle and bottom scatterplots contain parameter combinations with delayed transport and enhanced transport only, allowing the

regions of the parameter space associated with enhanced and delayed transport to be easily identified. Parameter combinations with enhanced transport are in the red color spectrum, delayed transport are in the blue color spectrum, and parameter combinations where pore water had little effect on transport fade to white. These 3D scatterplots are collapsed into 2D projections in Fig. 9 for D_d versus D^* (top), S versus D^* (middle), and S versus D_d (bottom). In other words, the dimension of one of the factors is collapsed onto the 2D plane of the other factors in each case (i.e., the S dimension is collapsed onto the D_d versus D^* plane in the top plot). The color spectrum for transport enhancement is identical in Figs. 8 and 9.

Transport enhancement due to the existence of pore water is most sensitive to the dissolution coefficient D_d with a Pearson's correlation coefficient of 0.63, while the diffusion coefficient and saturation have Pearson's correlation coefficients of 0.19 and 0.14, respectively. The dependence on saturation is as expected, increasing saturation provides increased capacity for the aqueous phase to enhance or delay transport. Gas transport is highly dependent on the combination of gaseous diffusion and dissolution coefficients as there is a clear delineation between diffusion/dissolution coefficient combinations that result in enhanced or retarded transport (top plot of Fig. 9). In the middle and bottom plots, where gaseous diffusion and dissolution coefficients, respectively, are plotted along the x-axis, it is apparent that, consistent with the Pearson's correlation coefficients, transport enhancement is more sensitive to the dissolution coefficient, which shows a more defined delineation between enhanced and delayed transport.

5 Discussion

The formulation and results presented here can be used to evaluate the effects of immobile pore-water storage on transport for different gases under different scenarios. Under idealized purely diffusive or advective transport, immobile pore-water storage retards gas transport with sufficiently large dissolution rate (refer to Figs. 3 and 4). However, in the presence of oscillatory flow (e.g., barometric pumping), immobile pore-water storage can either enhance or retard gas transport in fractured rock based on the gaseous diffusion and dissolution coefficients (top plot of Fig. 9 where enhanced and delayed transport parameter combinations are clearly delineated).

Many of the gases associated with the applications mentioned above have free-air diffusion coefficients slightly greater than 10^{-5} m^2/s at 20 °C (e.g., $D^*(CO_2) = 10^{-4.80}$, $D^*(CH_4) = 10^{-4.97}$, $D^*(Xe–N_2) = 10^{-4.91}$ m^2/s) (Haynes 2014)). Increasing the temperature will increase these values, but by only approximately a factor of 2 by 100 °C. The tortuosity of porous media will decrease the effective diffusivity. While many factors will influence dissolution coefficients (e.g., temperature, salinity), if we assume that the effective dissolution rate cannot be larger than free-water diffusion rate, the effective dissolution coefficients in many of the applications above will be at least less than around 10^{-9} m^2/s (e.g., $D_{aq}(CO_2) = 10^{-8.78}$, $D_{aq}(CH_4) = 10^{-8.79}$, $D_{aq}(Xe) = 10^{-8.90}$ m^2/s) (Haynes 2014)). While increases in temperature will increase these values, many other factors could result in lower effective dissolution coefficients, such as salinity, boundary layer effects, etc.

Taking the gaseous diffusion and dissolution coefficients above within the context of Fig. 9, our results suggest that tortuosity will have to decrease the effective diffusion coefficient and the effective dissolution coefficient will have to be several of orders of magnitude smaller than the free-water diffusion of the gas for significant enhanced transport in fractured rock

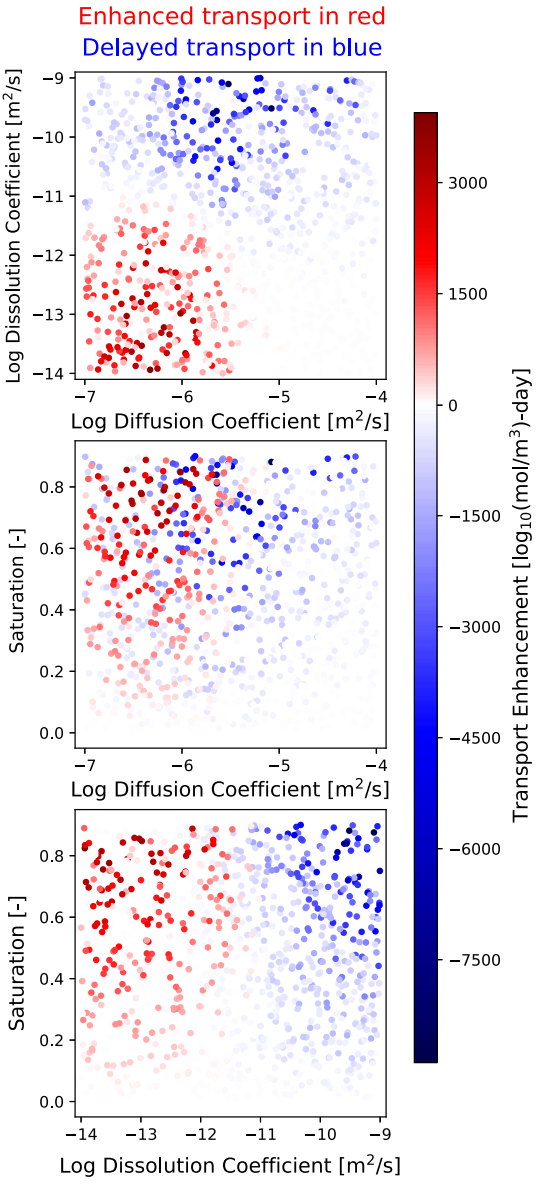

Fig. 9 Scatterplots of 2D projections through the LHS ensemble colored by pore-water transport enhancement for dissolution coefficient versus diffusion coefficient (top), saturation versus diffusion coefficient (middle), and saturation versus dissolution coefficient (bottom). Darker shades of red indicate greater transport enhancement, darker shades of blue indicate greater transport delay, and cases with little effect on transport fade to white

to occur due to the presence of pore water. Otherwise, our results suggest that transport will be retarded, and potentially significantly so, or will be unaffected. Knowledge of the effective gaseous diffusion and effective dissolution coefficients (and level of saturation) for a particular scenario (temperature, pressure, salinity, tortuosity, etc.) may be necessary to determine if enhanced or delayed transport in the fracture will occur.

This finding is contrary to the common assumption that pore water will always result in enhanced transport due to a ratcheting mechanism (Neeper and Stauffer 2012). Our results indicate that, while that may be true for particular scenarios, significant retardation of transport or negligible effect may occur for other scenarios. In fact, our results suggest that with little

tortuosity and an effective dissolution coefficient within a couple of orders of magnitude of the free-water diffusion of gas, the transport will be retarded.

Our results also call into question the assumption of "instantaneous equilibrium" often invoked for dissolution processes in numerical solvers, which assumes that the gas and aqueous concentrations equilibrate instantaneously at each time step (D_d effectively approaches infinity). Simulated gas concentrations are significantly different given different dissolution coefficients when saturations are high. For example, in the case of pure diffusion in Fig. 3, the relative concentration at the outlet of the model (depth=0) for $\phi_w = 0.9$ is more than 3 orders of magnitude less for $D_d = 10^{-10}$ than for $D_d = 10^{-14}$ m^2/s. In the case of pure advection in Fig. 4, variation of the dissolution coefficient from $D_d = 10^{-10}$ to 10^{-15} m^2/s changes the character of the transport from retarded without dispersion ($D_d = 10^{-10}$ m^2/s) to retarded with dispersion ($D_d = 10^{-13}$ m^2/s) to non-retarded ($D_d = 10^{-15}$ m^2/s), with significant differences in dispersion for the gas plume for higher saturations (i.e., higher values of ϕ_w). And, the top plot of Fig. 9 indicates that the gaseous diffusion and dissolution coefficients may determine if gas transport in the presence of pore water will be enhanced, retarded, or unaffected. Therefore, the assumption of instant equilibrium will be invalid for many gas transport applications. The assumption of "instantaneous equilibrium" has been found to be invalid for other mass transfer phenomenon as well. For example, Brusseau (1991) also found that the "instantaneous equilibrium" assumption applied to sorption is often invalid for gas transport applications.

6 Conclusions

We draw the following conclusions based on our simulations:

1. Immobile pore-water storage can enhance, retard, or have negligible effect on gas transport in fractured rock during oscillatory flow, contrary to existing knowledge that it can only enhance transport.
2. Dissolution coefficients less than around 10^{-11} m^2/s coupled with diffusion coefficients less than around 10^{-5} m^2/s lead to enhanced transport due to immobile pore-water storage during oscillatory flow.
3. Dissolution coefficients greater than around 10^{-11} m^2/s lead to delayed transport due to immobile pore-water storage during oscillatory flow.
4. Other combinations of dissolution and diffusion coefficients result in little effect of pore water on gas transport during oscillatory flow.
5. The degree of gas transport retardation due to immobile pore-water storage for *pure diffusion* is highly dependent on the dissolution coefficient.
6. The degree of gas transport retardation and plume dispersion due to immobile pore-water storage for *pure advection* is highly dependent on the dissolution coefficient.
7. The "instantaneous equilibrium" assumption for dissolution will fail to capture the nuances of immobile pore-water storage retardation and enhancement of gas transport.

Acknowledgements Funding for this work is provided by National Nuclear Security Administration Office of Defense Nuclear Nonproliferation Research and Development and the Defense Threat Reduction Agency under Interagency Agreement number HDTRA1825370 (DTRA10027 25370) as work for others. This research used resources provided by the Los Alamos National Laboratory Institutional Computing Program. Los Alamos National Laboratory completed this work under the auspices of the U.S. Department of Energy under contract DE-AC52-06NA24596.

A Benchmarking of Gas Transport Formulation

Since this is the first application of PFLOTRAN to model gas transport during barometric pumping, in the following section we benchmark the formulation to existing analytical solutions of gas transport and barometric pumping.

A.1 Gas Diffusion

Assuming a 1D vertical model and that Darcy (volumetric) flux q_z is zero, the concentration source and sink Q_c is zero, tortuosity τ is 1, and air-filled porosity ϕ_a is uniform, Eq. 4 can be simplified to

$$\frac{\partial C_g}{\partial t} = D^* \frac{\partial^2 C_g}{\partial z^2}. \tag{12}$$

If we consider a semi-infinite model with initial and boundary conditions of

$$\begin{aligned} \text{i.c.:} & C_g = 0 \text{ at } t = 0, z \geq 0, \\ \text{b.c. 1:} & C_g = C_{g,0} \text{ at } t > 0, z = 0, \\ \text{b.c. 2:} & C_g = 0 \text{ at } t > 0, z = \infty, \end{aligned} \tag{13}$$

the following well-known analytical solution describes the diffusive gas transport (Carslaw and Jaeger 1959, equation 10 on page 60)

$$C_g(z,t) = C_{g,0} \text{erfc}\left(\frac{z}{2\sqrt{D^* t}}\right), \tag{14}$$

where erfc is the complimentary error function. We created a corresponding simulation in PFLOTRAN with a 100-m vertical column composed of 10,000 uniformly spaced cells ($\Delta z = 0.01$ m). The maximum time step in PFLOTRAN is set at $\sim$9 h (0.001 years). Figure 10 compares relative concentrations of the two solutions in time series at 25, 50, and 75 m from the point source (left plot) and transects at 2.5, 5, 7.5, and 10 years (right plot). The fit in the plots verifies that our approach is consistent with the 1D gas diffusion analytical solution.

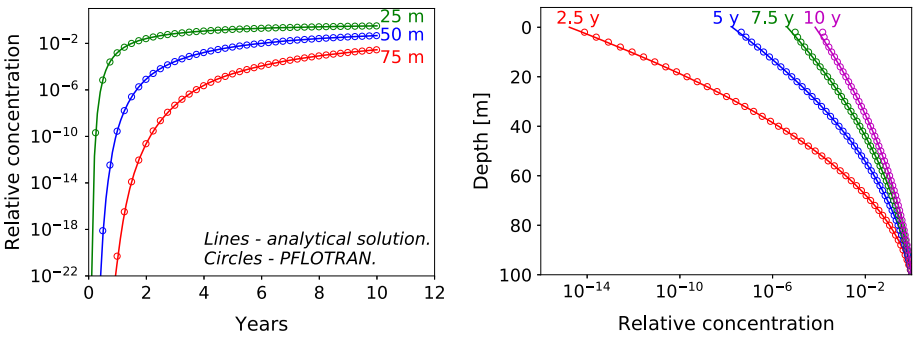

Fig. 10 Gas diffusion benchmark of our approach to a 1D diffusion analytical solution with a constant point source. Time series of relative concentrations labeled with distance from the point source are compared in the left plot. Transects of relative concentration over depth (depth $= 100 - z$) labeled with time are compared in the right plot. Lines are the analytical solution and circles are the PFLOTRAN solution

A.2 Gas Advection

Assuming uniform Darcy (volumetric) flux in the horizontal direction q_x, zero source or sink Q_c, tortuosity τ of 1, uniform air-filled porosity ϕ_a, and zero molecular diffusion and dispersion ($D^* = 0$), Eqs. 1 and 4 simplify to

$$\phi_a \frac{\partial \rho_a}{\partial t} = -\frac{\partial q_x \rho_a}{\partial x} \tag{15}$$

and

$$\phi_a \frac{\partial C_g}{\partial t} = -\frac{\partial^2 q_x C_g}{\partial x^2}, \tag{16}$$

respectively. If we consider an initial release of gas within the first upstream 10 m of the model, as described by initial and boundary conditions of

$$\begin{aligned} \text{i.c.:} & C_g = C_{g,0} \text{ at } t = 0, 0 < x < 10, \\ \text{b.c. 1:} & C_g = 0 \text{ at } t > 0, x = 0, \\ \text{b.c. 2:} & C_g = 0 \text{ at } t > 0, x = 100, \end{aligned} \tag{17}$$

the following solution describes purely advective flow:

$$C_g(x,t) = \begin{cases} C_{g,0}, & \text{if } 0 \le x - u * t \le 10 \\ 0, & \text{otherwise.} \end{cases} \tag{18}$$

Numerical solutions of the ADE (Eq. 4) are known to suffer from numerical dispersion. While previous investigations have focused on numerical dispersion in aqueous systems, an analysis involving gas transport is important here given the faster flow rates of gases in fractured rock. The Courant number,

$$Co = \frac{\Delta t q_x}{\Delta x}, \tag{19}$$

is a commonly used metric to determine if numerical dispersion will be significant for a given time step size Δt, velocity q_x, and mesh spacing Δx. While previous investigations have focused on numerical dispersion in aqueous systems, the following analysis is important given the faster flow rates of gases in fractured rock.

We evaluate the use of the Courant number for estimating numerical dispersion for our approach by estimating the apparent macrodispersivity of PFLOTRAN simulations with various Courant numbers. We ran PFLOTRAN simulations based on Eqs. 15 and 16 and initial and boundary conditions defined in equation 17 for all permutations of the following factors: (1) 1, 5, and 10 mm mesh spacing; (2) 1,10, and 100 h time step, and (3) 0.01, 0.1, and 1 $m^3/d/m^2$ uniform volumetric flux q_x (note that these are equal to pore velocities (m/s) in this case because $\phi_a = 1$), corresponding to Courant numbers ranging from $\sim$ 0.042 to $\sim$ 4200.

Macrodispersivity can be estimated based on the spatial extent of the plume (Dagan 1990) as

$$a = \frac{1}{2q_x} \frac{\partial(\sigma_x^2)}{\partial t}, \tag{20}$$

where σ_x^2 is the spatial variance of the plume, which is calculated based on spatial moments of the gas plume as

$$\sigma_x^2(t) = \frac{1}{C_T} \int x^2 C(x,t) dx - \mu_x^2(t), \tag{21}$$

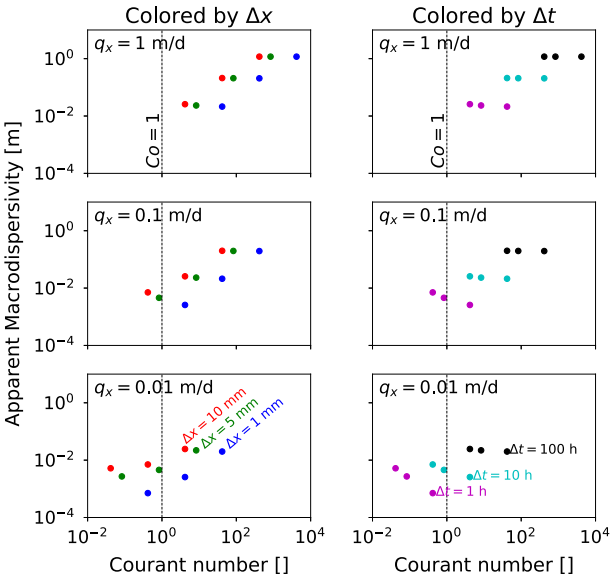

Fig. 11 Apparent macrodispersivity due to numerical dispersion as a function of Courant number for combinations of velocity q_x, mesh discretization Δx, and time step size Δt

where $C_T = \int C(x)dx$ and μ_x is the spatial mean of the plume calculated as

$$\mu_x(t) = \frac{1}{C_T} \int x C(x,t) \mathrm{d}x. \tag{22}$$

In order to estimate the variance due to numerical dispersion $\sigma^2_{x,n}$, the variance of purely advective flow, estimated by the uniform distribution, $\sigma^2_{x,a}(t) = \frac{(x_{max}(t) - x_{min}(t))^2}{12}$ is subtracted from σ^2_x

$$\sigma^2_{x,n}(t) = \sigma^2_x(t) - \sigma^2_{x,a}(t). \tag{23}$$

Substituting Eq. 23 into 20 for σ^2_x gives the apparent macrodispersivity due to numerical dispersion as

$$a_n = \frac{1}{2q_x} \frac{\partial(\sigma^2_{x,n})}{\partial t}. \tag{24}$$

Figure 11 contains plots of the apparent dispersivity due to numerical dispersion as a function of Courant number. The circles in the left and right columns of plots are colored by Δx and Δt, respectively, and q_x decreases down the rows of plots. The general rule that smaller Co results in less numerical dispersion is supported by Fig. 11 as Co and a_n both increase with increasing Δt and q_x; however, increasing Δx increases a_n, contrary to the rule defined by the Courant number (Eq. 19). Therefore, the contrary effect of Δx when using the Courant number as an indicator of numerical dispersion must be considered.

Figure 12 contains plots of relative concentration transects for the models with large and small numerical dispersion for $q_x = 0.01,\ 0.1,\ 1\ \mathrm{m^3/d/m^2}$. The purely advective transport of gas has reached the same location ($\sim$ 46.5 m) for each uniform velocity q_x, but at different times. Based on these plots, it is possible to approach the analytical solution, but this requires small Δx and Δt. Mitigation of numerical dispersion for meter per day flow rates, while possible through increased spatial and temporal discretization, may be computationally

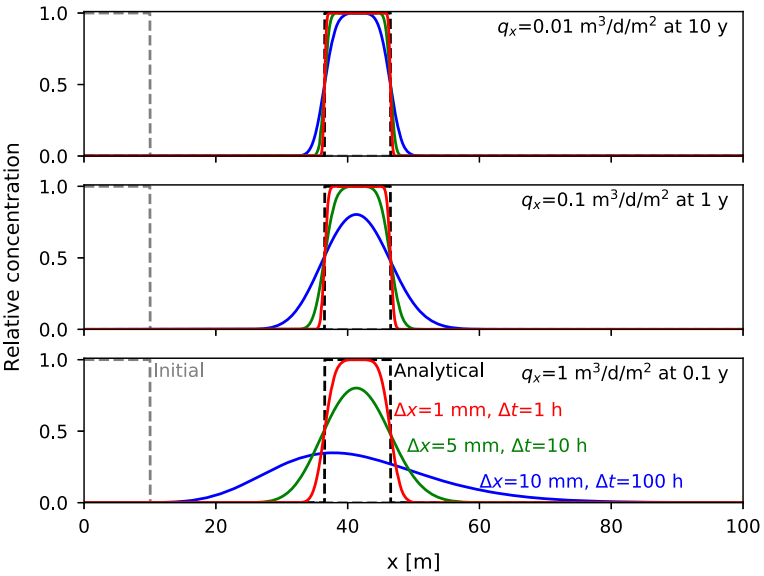

Fig. 12 Comparison of numerical approach to analytical solution of purely advective gas transport. The rows of plots present results for uniform flow rates of $u = 0.01$, 0.1, and 1 m/d and times of 10, 1, and 0.1 years, respectively. The initial concentration for all models is shown as a dashed gray line, and the analytical solution in each scenario is shown as a black dashed line. The colored lines in each plot are for combinations of spatial discretization Δx and time step size Δt labeled in the bottom plot

challenging for large models. Implementation of higher order solutions of Eq. 4 (Lax and Wendroff 1960; Liu et al. 1994) or particle tracking approaches (Painter et al. 2012) could be used to reduce the numerical dispersion and should be explored further for modeling gas transport in fractured rock.

A.3 Sinusoidal Pressure Pumping of a Fracture

The ability to capture pressure changes during oscillatory flow is critical for modeling gas transport in fractured rock. Therefore, we benchmark our approach to a dual-porosity analytical solution of barometric pumping by Nilson et al. (1991) who introduced the following equations for laminar fracture flow with diffusive walls of finite thickness:

$$\frac{\partial p}{\partial t} = \alpha_{\mathrm{f}} \frac{\partial^2 p}{\partial z^2} + 2 \frac{\phi_{\mathrm{m}} \alpha_{\mathrm{m}}}{\delta_{\mathrm{f}}} \frac{\partial p}{\partial x} \tag{25}$$

and

$$\frac{\partial p}{\partial t} = \alpha_{\mathrm{m}} \frac{\partial^2 p}{\partial x^2}, \tag{26}$$

where ϕ_{m} is the air-filled porosity of the matrix, and δ_{f} is the fracture aperture, and α_{f} and α_{m} are the pneumatic diffusivities of the fracture and matrix expressed as

$$\alpha_{\mathrm{f}} = \frac{\delta_{\mathrm{f}}^2 \overline{p}_0}{12\mu} \tag{27}$$

and

$$\alpha_{\mathrm{m}} = \frac{k_{\mathrm{m}} \overline{p}_0}{\mu \phi_{\mathrm{m}}}, \tag{28}$$

respectively, where $\overline{p}_0$ is the average barometric pressure and k_{m} is the matrix permeability. Equation 27 is derived from the cubic law (Witherspoon et al. 1980) for transmissivity describing laminar flow within parallel planar fractures (expressed as $k = \delta_{\mathrm{f}}^2/12$ in terms of permeability).

Assuming that the change in barometric pressure is much smaller than the magnitude of the barometric pressure ($\Delta p \ll \overline{p}_0$) and applying a sinusoidal pressure boundary condition at $z = 0$ ($p = \overline{p}_0 + \Delta p e^{i\omega t}$, where $i = (1+i)/\sqrt{2}$ and ω is frequency), Nilson et al. (1991) provide the following solution to Eqs. 25 and 26:

$$\frac{p - \overline{p}_0}{\Delta p} = \frac{\cosh \lambda_{fm} \sqrt{i}(1 - z/L)}{\cosh \lambda_{fm} \sqrt{i}} \frac{\cosh \lambda_{\mathrm{m}} \sqrt{i}(1 - 2x/\delta_{\mathrm{m}})}{\cosh \lambda_{\mathrm{m}} \sqrt{i}} e^{i\omega t}, \tag{29}$$

where δ_{m} is matrix block width and L is the depth to an impermeable material (impermeable bedrock or water table). λ_{fm}, λ_{f}, and λ_{m} are Fourier numbers for fracture/matrix, fracture, and matrix, respectively, defined as

$$\lambda_{fm} = \lambda_{\mathrm{f}} \left(1 + \frac{\phi_{\mathrm{m}} \delta_{\mathrm{m}}}{\delta_{\mathrm{f}}} \frac{\tanh \lambda_{\mathrm{m}} \sqrt{i}}{\lambda_{\mathrm{m}} \sqrt{i}} \right)^{1/2}, \tag{30}$$

$$\lambda_{\mathrm{f}} = L \sqrt{\frac{\omega}{\alpha_{\mathrm{f}}}}, \tag{31}$$

and

$$\lambda_{\mathrm{m}} = \frac{\delta_{\mathrm{m}}}{2} \sqrt{\frac{\omega}{\alpha_{\mathrm{m}}}}. \tag{32}$$

We created a corresponding 2D PFLOTRAN model according to Eqs. 25 and 26 with a single column of cells representing the half-fracture with 0.05 mm width (representing a 0.1-mm fracture aperture via symmetry about a reflection boundary along $x = 0$) with increasing log spacing in the horizontal direction away from the vertical fracture to 5 m and uniform vertical mesh spacing of 0.01 m. As with the analytical solution, the permeability of the fracture is determined from the aperture based on the cubic law and is 8.3×10^{-10} m^2, while the permeability of the matrix is 10^{-17} m^2. A sinusoidal barometric pressure boundary condition is applied to both models at the top of the fracture with 1000 Pa amplitude and 7.305 day period. The remaining boundaries are no flow. The model is initialized with uniform pressure and spun up until it matches the analytical solution which converges quickly after a few barometric cycles.

The compressibility β in the analytical solution (indirectly represented here; see discussion below) comes from the following relationship:

$$\beta = \frac{1}{V} \left(\frac{\mathrm{d}V}{\mathrm{d}p} \right)_T, \tag{33}$$

where V is volume and T is temperature. Substituting the ideal gas law in terms of V as

$$V = nRTp^{-1} \tag{34}$$

and its derivative with respect to p as

$$\left(\frac{dV}{dp} \right)_T = -nRTp^{-2}, \tag{35}$$

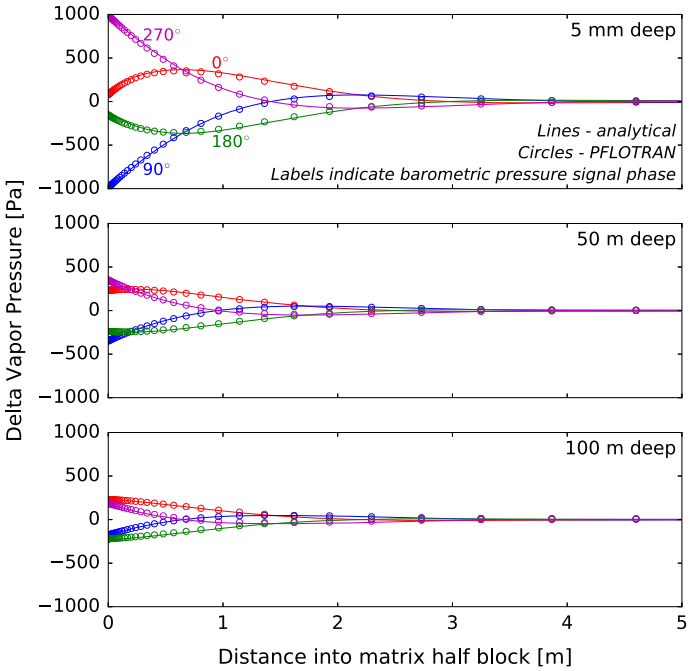

Fig. 13 Comparison of barometric pumping of a 100-m deep, 0.1-mm vertical fracture connected to a 5-m matrix half-block with 10^{-17} m^2/s permeability. Horizontal delta pressure transects from the fracture through the matrix half-block are presented at 5 mm, 50, and 100 m depths in the top, middle, and bottom plots, respectively. The barometric pressure signal is sinusoidal with 1000 Pa amplitude and 7.305 d period. The lines and circles are delta pressures calculated using the analytical solution from Nilson et al. (1991) and PFLOTRAN, respectively. Labels in the top plot indicate the phase of the delta barometric pressure signal where 0° is at a delta vapor pressure of zero and decreasing

where n is the number of moles, and R is the universal gas constant, into Eq. 33, canceling terms, and replacing p with $\overline{p}_0$ produces $\beta = 1/\overline{p}_0$. This relationship is implied in Eqs. 27 and 28 where $\overline{p}_0$ is in the numerator (i.e., the $\overline{p}_0$ in the numerator could be replaced by β in the denominator). The compressibility is set to the same value $(1/\overline{p}_0)$ in PFLOTRAN in Eq. 3. In PFLOTRAN, density is a function of pressure, while in the analytical solution, it is not. Since in most scenarios of interest (and in the benchmarking problem here) $\Delta p \ll \overline{p}_0$, the density between the numerical and analytical solutions are not significantly different. Note that since the analytical solution is a single-phase solution without pore-water storage, the saturation in the PFLOTRAN simulation has been set to zero.

Figure 13 contains plots of horizontal delta vapor pressure transects through the matrix at 5 mm, 50, and 100 m depths for pressure signal phases of 0°, 90°, 180°, and 270°, where the phase of 0° corresponds to a delta vapor pressure of 0 Pa and decreasing. The plots indicate that our approach is able to match the analytical solution of barometric pumping of a fracture.

A.4 Gas Migration Along a Fracture with Uniform Flow and Diffusive Walls

With non-oscillatory flow, gas diffusion into the rock matrix retards gas transport within fractures. Capturing this process is critical for accurately simulating gas breakthrough, particularly prior to gas saturation of the air- and water-filled porosities in the rock matrix. We

can simplify Eq. 4 to describe transport along a vertical fracture with uniform upward flow q_z and no axial dispersion as

$$\frac{\partial C_{\mathrm{g,f}}}{\partial t} + q_z \frac{\partial C_{\mathrm{g,f}}}{\partial z} = \phi_{\mathrm{m}} D^* \frac{\partial C_{\mathrm{g,m}}}{\partial x} \tag{36}$$

and diffusion into an infinitely thick matrix (the finite matrix block width δ_{m} is accounted for below in the formulation of the uniform velocity q_z) as

$$\frac{\partial C_{\mathrm{g,m}}}{\partial t} = D^* \frac{\partial^2 C_{\mathrm{g,m}}}{\partial x^2}, \tag{37}$$

where $C_{\mathrm{g,f}}$ and $C_{\mathrm{g,m}}$ are gas concentrations in the fracture and matrix, respectively, z is the fracture coordinate where there is a constant source of gas, $C_{\mathrm{g},0}$, at $z = 0$, x is the matrix coordinate where $x = 0$ is the fracture–matrix interface, and D^* is the molecular diffusion coefficient in the matrix only in this case. If we consider initial and boundary conditions of

$$\begin{aligned}
\text{i.c.:} & C_{\mathrm{g,f}} = C_{\mathrm{g,m}} = 0 \text{ at } t = 0, x > 0, z > 0, \\
\text{b.c. 1:} & C_{\mathrm{g,f}} = C_{\mathrm{g,m}} = C_{\mathrm{g},0} \text{ at } t > 0, x = 0, z = 0, \\
\text{b.c. 2:} & C_{\mathrm{g,f}} = C_{\mathrm{g,m}} \text{ at } t > 0, x = 0, z > 0, \\
\text{b.c. 3:} & C_{\mathrm{g,m}} = 0 \text{ at } t > 0, x > 0, z \to \infty,
\end{aligned} \tag{38}$$

the following well-known analytical solution exists for gas concentrations in the fracture for $t > x/q_z$ (Carslaw and Jaeger 1959, equation 38 on page 396; Grisak and Pickens 1981):

$$C_{\mathrm{g}} = C_{\mathrm{g},0} \mathrm{erfc}\left[\frac{z D^* \phi_{\mathrm{m}}}{q_z \delta_{\mathrm{f}} (D^*(t - z/q_z))^{1/2}}\right]. \tag{39}$$

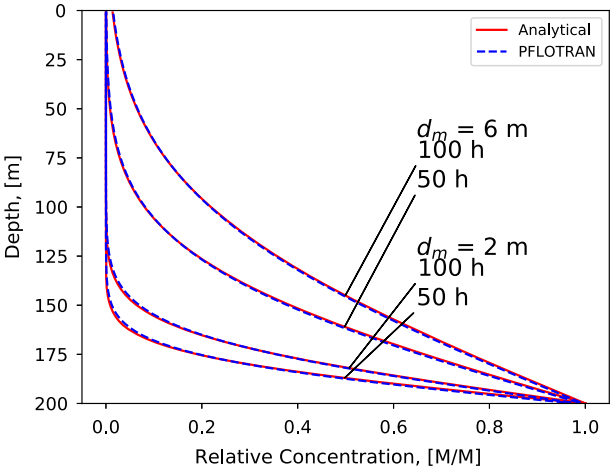

Fig. 14 Relative gas concentrations along vertical fractures with diffusive walls with a constant source of gas at the bottom of the fracture (200 m depth) and uniform flow up the fracture. Analytical and numerical concentration transects are plotted for matrix block widths of 6 and 2 m at 50 and 100 h. Nilson et al. (1991) present a similar plot of the analytical solution in Figure 9 of their paper

Following the approach of Nilson et al. (1991), the finite matrix block width can be accounted for in the calculation of the uniform velocity q_z as

$$q_z = \frac{2L_b\phi_m\delta_m}{T\delta_f}\frac{\delta p}{\overline{p}_0}, \tag{40}$$

where L_b is the thickness of contaminated ground below $z = 0$ and T is the period of the sinusoidal barometric pressure signal. Tang et al. (1981), Sudicky and Frind (1982) provide more advanced analytical solutions of gas transport in fractures.

Figure 14 contains a comparison of PFLOTRAN with Eqs. 39 and 40 at 50 and 100 h for matrix block widths of 2 and 6 m. A similar plot is shown in Figure 9 of Nilson et al. (1991) for the analytical solution only.

References

Auer, L.H., Rosenberg, N.D., Birdsell, K.H., Whitney, E.M.: The effects of barometric pumping on contaminant transport. J. Contam. Hydrol. **24**(2), 145–166 (1996). https://doi.org/10.1016/s0169-7722(96)00010-1

Bowyer, T.W., Schlosser, C., Abel, K.H., Auer, M., Hayes, J.C., Heimbigner, T.R., McIntyre, J.I., Panisko, M.E., Reeder, P.L., Satorius, H., et al.: Detection and analysis of xenon isotopes for the comprehensive nuclear-test-ban treaty international monitoring system. J. Environ. Radioact. **59**(2), 139–151 (2002)

Brusseau, M.L.: Transport of organic chemicals by gas advection in structured or heterogeneous porous media: development of a model and application to column experiments. Water Resour. Res. **27**(12), 3189–3199 (1991)

Carrigan, C.R., Sun, Y.: Detection of noble gas radionuclides from an underground nuclear explosion during a ctbt on-site inspection. Pure Appl. Geophys. **171**(3–5), 717–734 (2014)

Carrigan, C.R., Heinle, R.A., Hudson, G.B., Nitao, J.J., Zucca, J.J.: Trace gas emissions on geological faults as indicators of underground nuclear testing. Nature **382**(6591), 528–531 (1996). https://doi.org/10.1038/382528a0

Carrigan, C.R., Sun, Y., Hunter, S.L., Ruddle, D.G., Wagoner, J.L., Myers, K.B., Emer, D.F., Drellack, S.L., Chipman, V.D.: Delayed signatures of underground nuclear explosions. Sci. Rep. **6**(23), 032 (2016)

Carroll, S.A., Keating, E., Mansoor, K., Dai, Z., Sun, Y., Trainor-Guitton, W., Brown, C., Bacon, D.: Key factors for determining groundwater impacts due to leakage from geologic carbon sequestration reservoirs. Int. J. Greenh. Gas Control **29**, 153–168 (2014)

Carslaw, H.S., Jaeger, J.C.: Conduction of Heat in Solids, 2nd edn. Clarendon Press, Oxford (1959)

Chen, Z.X.: Transient flow of slightly compressible fluids through double-porosity, double-permeability systemsa state-of-the-art review. Transport Porous Media **4**(2), 147–184 (1989)

Dagan, G.: Transport in heterogeneous porous formations: spatial moments, ergodicity, and effective dispersion. Water Resourc. Res. **26**(6), 1281–1290 (1990)

Dempsey, D., Kelkar, S., Pawar, R.: Passive injection: a strategy for mitigating reservoir pressurization, induced seismicity and brine migration in geologic CO2 storage. Int. J. Greenh. Gas Control **28**, 96–113 (2014)

Ellerd, M.G., Massmann, J.W., Schwaegler, D.P., Rohay, V.J.: Enhancements for passive vapor extraction: the hanford study. Groundwater **37**(3), 427–437 (1999)

Grisak, G., Pickens, J.: An analytical solution for solute transport through fractured media with matrix diffusion. J. Hydrol. **52**(1–2), 47–57 (1981)

Hammond, G.E.: Pflotran: Recent developments facilitating massively-parallel reactive biogeochemical transport. Technical Report SAND2015-10867C, Sandia National Laboratories, Albuquerque, NM (2015)

Haynes, W.M.: CRC Handbook of Chemistry and Physics. CRC press, Boca Raton (2014)

Ho, C.K., Webb, S.W.: Gas Transport in Porous Media, vol. 20. Springer, Berlin (2006)

Hyman, J.D., Karra, S., Makedonska, N., Gable, C.W., Painter, S.L., Viswanathan, H.S.: dfnWorks: a discrete fracture network framework for modeling subsurface flow and transport. Comput. Geosci. **84**, 10–19 (2015)

Issartel, J.P., Baverel, J.: Inverse transport for the verification of the comprehensive nuclear test ban treaty. Atmos. Chem. Phys. **3**(3), 475–486 (2003)

Jordan, A.B., Stauffer, P.H., Zyvoloski, G.A., Person, M.A., MacCarthy, J.K., Anderson, D.N.: Uncertainty in prediction of radionuclide gas migration from underground nuclear explosions. Vadose Zone J. (2014). https://doi.org/10.2136/vzj2014.06.0070

Jordan, A.B., Stauffer, P.H., Knight, E.E., Rougier, E., Anderson, D.N.: Radionuclide gas transport through nuclear explosion-generated fracture networks. Sci. Rep. **5**(18), 383 (2015)
Lax, P., Wendroff, B.: Systems of conservation laws. Commun. Pure Appl. Math. **13**(2), 217–237 (1960)
Lichtner, P., Hammond, G., Lu, C., Karra, S., Bisht, G., Andre, B., Mills, R., Kumar, J.: PFLOTRAN user manual: A massively parallel reactive flow and transport model for describing surface and subsurface processes. Technial Report, Report No.: LA-UR-15-20403, Los Alamos National Laboratory (2015)
Liu, X.D., Osher, S., Chan, T.: Weighted essentially non-oscillatory schemes. J. Comput. Phys. **115**(1), 200–212 (1994)
Myers, T.: Potential contaminant pathways from hydraulically fractured shale to aquifers. Groundwater **50**(6), 872–882 (2012)
Neeper, D.A.: Investigation of the vadose zone using barometric pressure cycles. J. Contam. Hydrol. **54**(1–2), 59–80 (2002). https://doi.org/10.1016/s0169-7722(01)00146-2
Neeper, D.A., Stauffer, P.: Unidirectional gas flow in soil porosity resulting from barometric pressure cycles. J. Contam. Hydrol. **78**(4), 281–289 (2005)
Neeper, D.A., Stauffer, P.H.: Transport by oscillatory flow in soils with rate-limited mass transfer: 1. theory. Vadose Zone J. (2012). https://doi.org/10.2136/vzj2011.0093
Nilson, R., Lie, K.: Double-porosity modelling of oscillatory gas motion and contaminant transport in a fractured porous medium. Int. J. Numer. Anal. Methods Geomech. **14**(8), 565–585 (1990)
Nilson, R.H., Peterson, E.W., Lie, K.H., Burkhard, N.R., Hearst, J.R.: Atmospheric pumping: a mechanism causing vertical transport of contaminated gases through fractured permeable media. J. Geophys. Res. **96**(B13), 21,933–21,948 (1991). https://doi.org/10.1029/91jb01836
Noyes, A.A., Whitney, W.R.: The rate of solution of solid substances in their own solutions. J. Am. Chem. Soc. **19**(12), 930–934 (1897)
Oldenburg, C.M., Unger, A.J.: On leakage and seepage from geologic carbon sequestration sites. Vadose Zone J. **2**(3), 287–296 (2003)
Painter, S., Gable, C., Kelkar, S.: Pathline tracing on fully unstructured control-volume grids. In: Computational Geosciences, pp. 1–10 (2012)
Pan, L., Oldenburg, C.M., Pruess, K., Wu, Y.S.: Transient co2 leakage and injection in wellbore-reservoir systems for geologic carbon sequestration. Greenh. Gases: Sci. Technol. **1**(4), 335–350 (2011)
Rathfelder, K., Lang, J., Abriola, L.: Soil vapor extraction and bioventing: applications, limitations, and future research directions. Rev. Geophys. **33**(S2), 1067–1081 (1995)
Shukla, R., Ranjith, P., Haque, A., Choi, X.: A review of studies on co_2 sequestration and caprock integrity. Fuel **89**(10), 2651–2664 (2010)
Stauffer, P.H., Birdsell, K.H., Witkowski, M.S., Hopkins, J.K.: Vadose zone transport of 1, 1, 1-trichloroethane. Vadose Zone J. **4**(3), 760–773 (2005)
Sudicky, E., Frind, E.: Contaminant transport in fractured porous media: analytical solutions for a system of parallel fractures. Water Resour. Res. **18**(6), 1634–1642 (1982)
Sun, Y., Carrigan, C.: Modeling noble gas transport and detection for the comprehensive Nuclear-Test-Ban Treaty. Pure Appl. Geophys. **171**(3–5), 735–750 (2014). https://doi.org/10.1007/s00024-012-0514-4
Tang, D., Frind, E., Sudicky, E.A.: Contaminant transport in fractured porous media: analytical solution for a single fracture. Water Resour. Res. **17**(3), 555–564 (1981)
Viswanathan, H.S., Pawar, R.J., Stauffer, P.H., Kaszuba, J.P., Carey, J.W., Olsen, S.C., Keating, G.N., Kavetski, D., Guthrie, G.D.: Development of a hybrid process and system model for the assessment of wellbore leakage at a geologic co2 sequestration site. Environ. Sci. Technol. **42**(19), 7280–7286 (2008)
Witherspoon, P.A., Wang, J.S., Iwai, K., Gale, J.E.: Validity of cubic law for fluid flow in a deformable rock fracture. Water Resour. Res. **16**(6), 1016–1024 (1980)
Wyatt, D., Richers, D., Pirkle, R.: Barometric pumping effects on soil gas studies for geological and environmental characterization. Environ. Geol. **25**(4), 243–250 (1995)